
Cometh: A continuous-time discrete-state graph diffusion model

Antoine Siraudin
RWTH Aachen University
antoine.siraudin@log.rwth-aachen.de

Fragkikos D. Malliaros
Université Paris-Saclay
CentraleSupélec
Inria

Christopher Morris
RWTH Aachen University

Abstract

Discrete-state denoising diffusion models led to state-of-the-art performance in graph generation, especially in the molecular domain. Recently, they have been transposed to continuous time, allowing more flexibility in the reverse process and a better trade-off between sampling efficiency and quality. Here, to leverage the benefits of both approaches, we propose COMETH, a continuous-time discrete-state graph diffusion model, integrating graph data into a continuous-time diffusion model framework. Empirically, we show that integrating continuous time leads to significant improvements across various metrics over state-of-the-art discrete-state diffusion models on a large set of molecular and non-molecular benchmark datasets.

1 Introduction

Denoising diffusion models [Ho et al., 2020, Song et al., 2020] are among the most prominent and successful classes of generative models. Intuitively, these models aim to denoise diffusion trajectories and produce new samples by sampling noise and recursively denoising it, often outperforming competing architectures in tasks such as image and video generation [Sohl-Dickstein et al., 2015, Yang et al., 2023]. Recently, a large set of works, e.g., Chen et al. [2023], Jo et al. [2022, 2024], Vignac et al. [2022], aimed to leverage diffusion models for *graph generation*, e.g., the generation of molecular structures. One class of such models embeds the graphs into a continuous space and adds Gaussian noise to the node features and graph adjacency matrix [Jo et al., 2022]. However, such noise destroys the graph’s sparsity, resulting in complete, noisy graphs without meaningful structural information, making it difficult for the denoising network to capture the structural properties of the data. Therefore, *discrete-state* graph diffusion models such as DIGRESS [Vignac et al., 2022] have been proposed, exhibiting competitive performance against their continuous-state counterparts.

In parallel, Gaussian-noise-based diffusion models have been extended to *continuous time* [Song et al., 2020] by formulating the forward process as a stochastic differential equation. In addition, discrete-state diffusion models have recently been transposed to continuous time [Campbell et al., 2022, Sun et al., 2022], relying on *continuous-time Markov chains* (CTMC). Unlike their discrete-time counterparts, which define a fixed time scale during training, they allow training using a continuous-time scale and leave the choice of the time discretization strategy for the sampling stage. Hence, the integration of continuous time allows for more flexibility in the design of the reverse process and a better trade-off between sampling efficiency and quality.

Present work Here, to leverage the benefits of both approaches, i.e., discrete-state and continuous-time, we propose COMETH, a continuous-time discrete-state graph diffusion model, integrating graph data into a continuous diffusion model framework; see Figure 1 for an overview of COMETH. Concretely, we

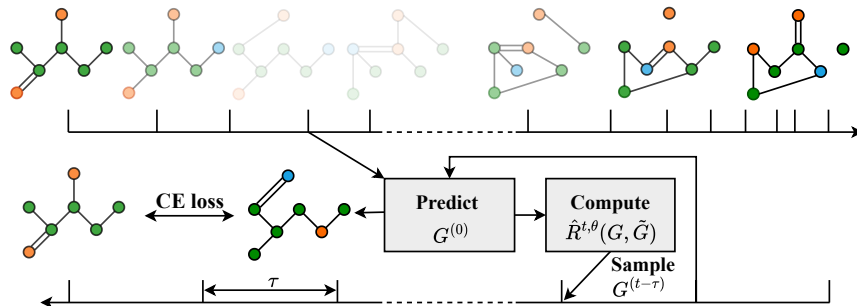


Figure 1: Overview of COMETH. During training, COMETH, unlike previous discrete-state diffusion models, transitions at any time $t \in [0, 1]$, while during sampling, the step length is fixed to τ . During sampling, we can additionally apply multiple corrector steps at $t - \tau$.

1. propose a new noise model adapted to graph specificities using different node and edge rates and a tailored marginal distribution and noise schedule.
2. In addition, we successfully replace the structural features of DiGRESS with a single random-walk-based encoding with provable expressivity guarantees, removing unnecessary features.
3. Empirically, we show that integrating continuous-time into a discrete-state graph diffusion model and leveraging a predictor-corrector mechanism leads to state-of-the-art results on synthetic and established molecular benchmark datasets across various metrics.

Overall, COMETH is the first graph diffusion model allowing the benefits of using a discrete-state space and the flexibility of a continuous-time scale in the design of the sampling algorithm.

Related work Diffusion models are a prominent class of generative models successfully applied to many data modalities, such as images, videos, or point clouds [Yang et al., 2023].

Graph generation is a well-studied task applied to a wide range of application domains, such as molecule generation, floorplan generation, or abstract syntax tree generation [Shabani et al., 2023, Shi et al., 2019]. We can roughly categorize graph generation approaches into *auto-regressive models* such as Kong et al. [2023], You et al. [2018] and *one-shot models* such as diffusion models. The main advantage of one-shot models over auto-regressive ones is that they generate the whole graph in a single step and do not require any complex procedure to select a node ordering. On the other hand, auto-regressive models are more flexible regarding the size of the generated graph, which can remain unknown beforehand, and they do not suffer from the quadratic complexity of one-shot models.

While the first diffusion models for graph generation leveraged continuous-state spaces [Niu et al., 2020], they are now largely replaced by discrete-state diffusion models [Haefeli et al., 2022, Vignac et al., 2022], using a discrete time scale. However, using discrete-time constrains the sampling scheme to a particular form called *ancestral sampling*, which prevents the exploration of alternative sampling strategies that could optimize sampling time or enhance sampling quality.

Another line of research considers lifting the graphs into a continuous-state space and applying Gaussian noise to the node and edge features matrices [Niu et al., 2020, Jo et al., 2022, 2024]. Such continuous noise allows the generation of continuous features to be handled smoothly, such as the generation of atomic coordinates in molecular graphs [Jo et al., 2024]. The above Gaussian-noise-based diffusion models have many successful applications in computational biology (Corso et al. [2023], Yim et al. [2023]). However, they almost exclusively consider point-cloud generation, focusing on modeling the geometry of the molecules and ignoring structural information. In addition, some hybrid approaches also exist that consider jointly modeling the 2D molecular graphs and their 3D geometry [Hua et al., 2024, Le et al., 2023, Vignac et al., 2023]. These models usually rely on continuous noise for the atomic coordinates and discrete noise for the atom and edge types.

Recent works have tried to scale graph generative models in size [Bergmeister et al., 2023, Luo et al., 2023, Qin et al., 2023]. Such frameworks are often built on top of previously proposed approaches, e.g., SPARSEDIFF [Qin et al., 2023] is based on DiGRESS. Therefore, these scaling methods are likely to apply to our approach.

2 Background

In the following, we introduce notations, and an overview of continuous-time discrete diffusion.

Notation In the following, let \mathcal{Z} , with cardinality $S := |\mathcal{Z}|$, be a *state space*, and $p_{\text{data}}(z_0)$ denotes the probability of sampling $z_0 \in \mathcal{Z}$. We superscript t to denote the noisy state $z^{(t)}$ at time t , and $t \in [0, T]$. By $\mathbf{1}$, we denote an all-one vector of appropriate size, by \mathbf{I} , the identity matrix of appropriate size, while $\mathbf{0}$ denotes the all-zero matrix of appropriate size. Moreover, by \mathbf{a}' , we denote the transpose of the vector \mathbf{a} .

Next, we overview the discrete-state continuous-time discrete-state diffusion framework on which COMETH builds. We provide a description of the discrete-state discrete-time diffusion model in appendix A.1, and refer to Yang et al. [2023] for a general introduction to diffusion models.

Continuous-time discrete diffusion Following the continuous-time generalization of diffusion models by Song et al. [2020], some recent works have considered applying continuous-time methods to discrete-state diffusion problems [Campbell et al., 2022, Sun et al., 2022]. Here, the discrete-time Markov chain of discrete diffusion models [Ho et al., 2020, Austin et al., 2021] is replaced by a *continuous-time Markov chain* (CTMC). The current state $z^{(t)}$ alternates between resting in the current state and transitioning to another state. A CTMC can be defined through a *transition rate matrix* $\mathbf{R}^{(t)} \in \mathbb{R}^{S \times S}$ and the initial data distribution $p_{\text{data}}(z^0)$. Intuitively, this matrix is analogous to the discrete-time transition matrix, but it contains instantaneous transition rates rather than transition probabilities. Formally, the *forward process* is defined as

$$q_{t+\Delta t|t}(\tilde{z} | z^{(t)}) := \delta_{\tilde{z}, z^{(t)}} + R^{(t)}(z^{(t)}, \tilde{z})\Delta t,$$

with $\delta_{\tilde{z}, z^{(t)}} = 1$ if $\tilde{z} = z^{(t)}$ and $R^{(t)}(z^{(t)}, \tilde{z})$ denotes the entry of $\mathbf{R}^{(t)}$ that gives the rate from $z^{(t)}$ to \tilde{z} . We provide details on the design of the rate matrix in appendix A.1.

As in the discrete-time case, we formulate a reverse CTMC admitting p_{ref} as an initial distribution and $p_{\text{data}}(z^{(0)})$ as a terminal distribution. The *reverse transition rate* $\hat{R}^{(t)}$ is untractable and has to be modeled by a parametrized approximation, i.e.,

$$\hat{R}^{t, \theta}(z, \tilde{z}) = R^{(t)}(\tilde{z}, z) \sum_{z^0} \frac{q_{t|0}(\tilde{z} | z^0)}{q_{t|0}(z | z^0)} p_{0|t}^{\theta}(z^0 | z), \text{ for } z \neq \tilde{z},$$

where $p_{0|t}^{\theta}(z^0 | z)$ is the *denoising neural network* with parameters θ . Since most real-world data is D -dimensional, for some $D > 1$, we need to extend the above unidimensional equations to the multi-dimensional case. A common assumption to handle D -dimensional data is to consider that the noise propagates independently over the dimensions to avoid considering a S^D -large state space. The forward process, thus, factorizes as $q_{t+\Delta t|t}(\tilde{z} | z) = \prod_{d=1}^D q_{t+\Delta t|t}(\tilde{z}_d | z_d)$ where $q_{t+\Delta t|t}(\tilde{z}_d | z_d)$ is the unidimensional forward process on the d th dimension. Following Campbell et al. [2022]), we can write the forward and reverse rates in D dimension as $R^{(t)}(\tilde{z}, z) = \sum_{d=1}^D \delta_{\tilde{z} \setminus d, z \setminus d} R_d^{(t)}(\tilde{z}_d, z_d)$ and $\hat{R}^{(t), \theta}(z, \tilde{z}) = \sum_{d=1}^D \delta_{\tilde{z} \setminus d, z \setminus d} R_d^{(t)}(\tilde{z}_d, z_d) \sum_{z_0} \frac{q_{t|0}(\tilde{z}_d | z_d^0)}{q_{t|0}(z_d | z_d^0)} p_{0|t}^{\theta}(z_d^0 | z_d)$ for $z_d \neq \tilde{z}_d$.

Synthetic samples can be produced by simulating the reverse process from $t = 0$ to $t = T$. Campbell et al. [2022] propose to use the tau-leaping algorithm in combination with the well-known predictor-corrector sampling scheme. Tau-leaping consists of holding the reverse rate constant as well as the current state for a time τ and then performing all the transitions that occur during this interval. The number of transitions in each dimension is Poisson distributed with mean $\tau \hat{R}^{t, \theta}(z_d, \tilde{z}_d)$.

3 Continuous-time Discrete Diffusion Model for Graph Generation

Here, we present our COMETH framework, a continuous-time discrete-state diffusion model for graph generation. Since changing T amounts to scale the time axis, we follow Campbell et al. [2022] and set $T = 1$. We denote n -order attributed graph as a pair $\mathbf{G} = (G, \mathbf{X}, \mathbf{E})$, where $G = (V(G), E(G))$ is a graph, $\mathbf{X} \in \mathbb{R}^{n \times a}$, for $a > 0$, is a *node feature matrix*, and $\mathbf{E} \in \mathbb{R}^{n \times n \times b}$, for $b > 0$, is an *edge feature tensor*. For notational convenience, in the following, we denote the graph at time $t \in [0, 1]$ by $\mathbf{G}^{(t)}$, the node feature of node $i \in V(G)$ at time t by $x_i^{(t)} \in \mathbb{R}^a$, and similarly the edge feature of edge

$(i, j) \in E(G)$ at time t by $e_{ij}^{(t)} \in \mathbb{R}^e$. In addition, we treat the absence of an edge as a special edge with a unique edge feature.

Forward process factorization Similarly to previous diffusion models, we consider that the forward process factorizes over dimensions and that the noise propagates independently on each node and edge, enabling us to consider node and edge state spaces separately rather than dealing with the much larger graph state space. Let $G = (G, \mathbf{X}, \mathbf{E})$ be n -order attributed graph, then we have

$$q_{t|0}(\mathbf{G}^{(t)} | \mathbf{G}^{(s)}) = \prod_i^n q_{t|0}(x_i^{(t)} | x_i^{(s)}) \prod_{i < j}^n q_{t|0}(e_{ij}^{(t)} | e_{ij}^{(s)}).$$

We then define a pair of rate matrices $(\mathbf{R}_X^{(t)}, \mathbf{R}_E^{(t)})$, with $\mathbf{R}_X^{(t)} := \beta(t)\mathbf{R}_X$ and $\mathbf{R}_E^{(t)} := \beta(t)\mathbf{R}_E$, where β is the noise schedule and $\mathbf{R}_X \in \mathbb{R}^{d \times d}$, $\mathbf{R}_E \in \mathbb{R}^{e \times e}$ are base rate matrices for nodes and edges, respectively. Given those rate matrices, we require an expression for the overall rate matrix. For that, we simply define $\mathbf{R}^{(t)}$ as the following $(d + e) \times (d + e)$ block diagonal matrix,

$$\mathbf{R}^{(t)} = \begin{bmatrix} \mathbf{R}_X^{(t)} & \mathbf{0} \\ \mathbf{0} & \mathbf{R}_E^{(t)} \end{bmatrix}.$$

It ensures that if $\mathbf{R}_X^{(t)}$ and $\mathbf{R}_E^{(t)}$ respect the necessary requirements to be transition rate matrices, then $\mathbf{R}^{(t)}$ respects them as well. In addition, since a node cannot transition to an edge and vice-versa, we can treat nodes and edges separately.

Noise model Most discrete diffusion models favor uniform distribution as the target distribution due to its apparent simplicity in modeling categorical data. Nevertheless, this choice is ill-suited for graphs, especially as a prior for the edge types distribution. Sampling edge types uniformly would yield a very dense graph for edge-attributed graphs, such as molecules. As most graphs are usually sparse, the model would need many denoising steps to reconstruct this sparsity.

Inspired by Vignac et al. [2022], COMETH diverges from the uniform noise model. We adopt the utilization of marginal node- and edge-type distributions as target distributions. In this context, the transition rate to a specific state is contingent upon its associated marginal probability, i.e., the more frequent a node or edge type is in the dataset, the higher the transition rate to this type.

Instead of employing the uniform rate matrix $\mathbf{R} = \mathbf{1}\mathbf{1}' - \mathbf{S}\mathbf{I}$, we use rate matrices comparable to the marginal transition matrix, i.e.,

$$\mathbf{R}_X = \mathbf{1}\mathbf{m}'_X - \mathbf{I} \quad \text{and} \quad \mathbf{R}_E = \mathbf{1}\mathbf{m}'_E - \mathbf{I},$$

where \mathbf{m}_X and \mathbf{m}_E are vectors representing the marginal distributions m_X and m_E of node and edge types, i.e., they contain the frequency of the different types in the dataset. Note that, by design, the rows of those transition rate matrices sum to zero.

Noise schedule Following Campbell et al. [2022], the forward process has the following expression,

$$q_{t|0}(x_i^{(t)} = k | x_i^{(0)} = l) = \left(\mathbf{Q}_X \exp \left[\mathbf{A}_X \int_0^t \beta(s) ds \right] \mathbf{Q}_X^{-1} \right)_{kl},$$

where $\mathbf{R}_X = \mathbf{Q}_X \mathbf{A}_X \mathbf{Q}_X^{-1}$ and \exp refers to the element-wise exponential. Similarly, for edges,

$$q_{t|0}(e_{ij}^{(t)} = k | e_{ij}^{(0)} = l) = \left(\mathbf{Q}_E \exp \left[\mathbf{A}_E \int_0^t \beta(s) ds \right] \mathbf{Q}_E^{-1} \right)_{kl}, \quad \text{if } i < j.$$

We can further refine this expression by using that $\mathbf{1}\mathbf{m}'$ is a rank-one matrix with trace 1, leading to the following result.

Proposition 1. For a CTMC $(z^{(t)})_{t \in [0,1]}$ with rate matrix $\mathbf{R}^{(t)} = \beta(t)\mathbf{R}_b$ and $\mathbf{R}_b = \mathbf{1}\mathbf{m}' - \mathbf{I}$, the forward process can be written as

$$\bar{\mathbf{Q}}^{(t)} = e^{-\bar{\beta}^{(t)}} \mathbf{I} + (1 - e^{-\bar{\beta}^{(t)}}) \mathbf{1}\mathbf{m}',$$

where $(\bar{\mathbf{Q}}^{(t)})_{ij} = q(z^{(t)} = i | z^0 = j)$ and $\bar{\beta}^{(t)} = \int_0^t \beta(s) ds$.

Proposition 1 gives us a clear understanding of how to design $\bar{\beta}^{(t)}$ to ensure that $\bar{\mathbf{Q}}^{(t)} \approx \mathbb{1}\mathbf{m}'$, so that the forward process converges to a permutation-invariant, easy-to-sample distribution. Even though, in theory, one should set $\lim_{t \rightarrow 1} \bar{\beta}^{(t)} = +\infty$ so that $\lim_{t \rightarrow 1} \bar{\mathbf{Q}}^{(t)} = \mathbb{1}\mathbf{m}'$, it considerably restricts the space of possible noise schedules. Relying on the exponentially decreasing behavior of the cumulative noise schedule $e^{-\bar{\beta}^{(t)}}$, one only needs to ensure that $\bar{\beta}^{(1)}$ is high enough so that $\bar{\mathbf{Q}}^{(1)}$ satisfyingly approximate $\mathbb{1}\mathbf{m}'$. Following an older heuristic regarding the choice of the noise schedule [Nichol and Dhariwal, 2021], we, therefore, propose to use a *cosine noise schedule*, where

$$\beta(t) = \alpha \frac{\pi}{2} \sin\left(\frac{\pi}{2}t\right) \quad \text{and} \quad \int_0^t \beta(s)ds = \alpha\left(1 - \cos\left(\frac{\pi}{2}t\right)\right).$$

Here, α is a constant factor. Given that α is high enough, the final forward process distribution will be close to $\mathbb{1}\mathbf{m}'$, and we can therefore use $\prod_i m_X \prod_{ij} m_E$ as our prior distribution. We provide the curve of our noise schedule in Appendix B.1.

Finally, noising a n -order attributed graph $\mathbf{G} = (\mathbf{G}, \mathbf{X}, \mathbf{E})$ amounts to sample from the following distribution,

$$q_{t|0}(\mathbf{G}^{(t)} | \mathbf{G}) = (\mathbf{X}\bar{\mathbf{Q}}_X^{(t)}, \mathbf{E}\bar{\mathbf{Q}}_E^{(t)}).$$

Since we consider only undirected graphs, we apply noise to the upper-triangular part of \mathbf{E} and symmetrize.

Parametrization & optimization We can formulate the approximate reverse rate for our graph generation model. For the unidimensional rates, we set

$$\begin{aligned} \hat{R}_X^{t,\theta}(x_i^{(t)}, \tilde{x}) &= R_X^t(\tilde{x}_i, x_i^{(t)}) \sum_{x_0} \frac{q_{t|0}(\tilde{x}_i | x_i^{(0)})}{q_{t|0}(x_i^{(t)} | x_i^{(0)})} p_{0|t}^\theta(x_i^{(0)} | \mathbf{G}^{(t)}), \text{ for } x_i^{(t)} \neq \tilde{x}_i, \\ \hat{R}_E^{t,\theta}(e_{ij}^{(t)}, \tilde{e}_{ij}) &= R_E^t(\tilde{e}_{ij}, e_{ij}^{(t)}) \sum_{e_0} \frac{q_{t|0}(\tilde{e}_{ij} | e_{ij}^{(0)})}{q_{t|0}(e_{ij}^{(t)} | e_{ij}^{(0)})} p_{0|t}^\theta(e_{ij}^{(0)} | \mathbf{G}^{(t)}), \text{ for } e_{ij}^{(t)} \neq \tilde{e}_{ij}. \end{aligned}$$

We elaborate on how to use those rates to simulate the reverse process in Section 3. Formally, we set the overall reverse rate to

$$\hat{R}^{t,\theta}(\mathbf{G}, \tilde{\mathbf{G}}) = \sum_i \delta_{\mathbf{G} \setminus x_i, \tilde{\mathbf{G}} \setminus x_i} \hat{R}_X^{t,\theta}(x_i^{(t)}, \tilde{x}) + \sum_{i < j} \delta_{\mathbf{G} \setminus e_{ij}, \tilde{\mathbf{G}} \setminus e_{ij}} \hat{R}_E^{t,\theta}(e_{ij}^{(t)}, \tilde{e}_{ij}),$$

where $\delta_{\mathbf{G} \setminus x_i, \tilde{\mathbf{G}} \setminus x_i}$ is 1 if \mathbf{G} and $\tilde{\mathbf{G}}$ differ only on node i , and similarly $\delta_{\mathbf{G} \setminus e_{ij}, \tilde{\mathbf{G}} \setminus e_{ij}}$ for edges. They exhibit the classic diffusion model parametrization, which relies on predicting a clean data point \mathbf{G} given a noisy input $\mathbf{G}^{(t)}$. We, therefore, train a denoising neural network $p_{0|t}^\theta(\mathbf{G} | \mathbf{G}^{(t)})$ to this purpose. The outputs are normalized into probability distributions for node and edge labels.

The model can be optimized using the continuous-time ELBO formulated in Campbell et al. [2022]. Given the similarities between the discrete and continuous-time optimization processes, we prefer to follow Vignac et al. [2022] and use the cross-entropy loss \mathcal{L}_{CE} as our optimization objective, i.e.,

$$\mathbb{E}_{t \sim \mathcal{U}([0,1]), p_{\text{data}}(\mathbf{G}^{(0)}), q(\mathbf{G}^{(t)} | \mathbf{G}^{(0)})} \left[- \sum_i^n \log p_{0|t}^\theta(x_i^{(0)} | \mathbf{G}^{(t)}) - \lambda \sum_{i < j}^n \log p_{0|t}^\theta(e_{ij}^{(0)} | \mathbf{G}^{(t)}) \right], \quad (1)$$

where $\lambda \in \mathbb{R}^+$ is a scaling factor that controls the relative importance of edges and nodes in the loss. In practice, we set $\lambda > 1$ so that the model prioritizes predicting a correct graph structure over predicting correct node types.

Neural Network & Encoding In all our experiments, we use the graph transformer proposed by Vignac et al. [2022]; see Figure 4 in the appendix. Relying on the fact that discrete diffusion models preserve the sparsity of noisy graphs, they propose a large set of features to compute at each denoising step to boost the expressivity of the model. This set includes Laplacian features, connected components features, and node- and graph-level cycle counts.

Even though this set of features has been successfully used in follow works, e.g., Vignac et al. [2023], Qin et al. [2023], Igashov et al. [2023], no theoretical nor experimental study exists to investigate the relevance of those particular features. In addition, a rich literature on encodings in graph learning has

been developed, e.g., LapPE [Kreuzer et al., 2021], SignNet [Lim et al., 2023], RWSE [Dwivedi et al., 2021], SPE [Huang et al., 2023], which led us to believe that powerful encodings developed for discriminative models should be transferred to the generative setting.

In our experiments, we leverage the *relative random-walk probabilities* (RRWP) encoding, introduced in Ma et al. [2023]. Denoting \mathbf{A} the adjacency matrix of a graph G , \mathbf{D} the diagonal degree matrix, and $\mathbf{M} = \mathbf{D}^{-1}\mathbf{A}$ the degree-normalized adjacency matrix, for each pair of nodes (i, j) , the RRWP encoding computes

$$P_{ij}^K := [I_{ij}, M_{ij}, M_{ij}^2, \dots, M_{ij}^{K-1}], \quad (2)$$

where K refers to the maximum length of the random walks. The entry P_{ii}^K corresponds to the RWSE encoding of node i ; therefore, we leverage them as node encodings. This encoding alone is sufficient to train our graph diffusion model and attain state-of-the-art results.

In the following, we show that RWPP encoding can (approximately) determine if two nodes lie in the same connected components and approximate the size of the largest connected component.

Proposition 2. For $n \in \mathbb{N}$, let \mathcal{G}_n denote the set of n -order graphs and for a graph $G \in \mathcal{G}_n$ let $V(G) := \llbracket 1, n \rrbracket$. Assume that the graph G has c connected components and let $\mathbf{C} \in \{0, 1\}^{n \times c}$ be a matrix such the i th row \mathbf{C}_i is a one-hot encoding indicating which of the c connected components the vertex i belongs to. Then, for any $\varepsilon > 0$, there exists a feed-forward neural network $\text{FNN}: \mathbb{R}^{n \times n} \rightarrow [0, 1]^{n \times c}$ such that

$$\|\text{FNN}(\mathbf{M}^{n-1}) - \mathbf{C}\|_F \leq \varepsilon.$$

Similarly, we can also approximate the size of the largest component in a given graph.

Proposition 3. For $n \in \mathbb{N}$, let \mathcal{G}_n denote the set of n -order graphs and for $G \in \mathcal{G}_n$ let $V(G) := \llbracket 1, n \rrbracket$. Assume that S is the number of vertices in the largest connected component of the graph G . Then, for any $\varepsilon > 0$, there exists a feed-forward neural network $\text{FNN}: \mathbb{R}^{n \times n} \rightarrow [1, n]$,

$$|\text{FNN}(\mathbf{M}^{n-1}) - S| \leq \varepsilon.$$

Moreover, we can show RRWP encodings can (approximately) count the number p -cycles, for $p < 5$, in which a node is contained. A p -cycle is a cycle on p vertices.

Proposition 4. For $n \in \mathbb{N}$, let \mathcal{G}_n denote the set of n -order graphs and for $G \in \mathcal{G}_n$ let $V(G) := \llbracket 1, n \rrbracket$. Assume that $c \in \mathbb{N}^n$ contains the number of p -cycles a node is contained in for all vertices in G , for $p \in \{3, 4\}$. Then, for any $\varepsilon > 0$, there exists a feed-forward neural network $\text{FNN}: \mathbb{R}^{n \times n} \rightarrow \mathbb{R}^n$,

$$\|\text{FNN}(\mathbf{P}^{n-1}) - \mathbf{c}\|_2 \leq \varepsilon.$$

However, we can also show that RRWP encodings cannot detect if a node is contained in a large cycle of a given graph. We say that an encoding, e.g., RRWP, counts the number of p -cycles for $p \geq 2$ if there do not exist two graphs, one containing at least one p -cycle while the other does not, while the RRWP encodings of the two graphs are equivalent.

Proposition 5. For $p \geq 8$, the RRWP encoding does not count the number of p -cycles.

Hence, the above proposition implies the following result.

Corollary 6. For $p \geq 8$ and $K \geq 0$, there exists a graph G containing a p -cycle C , and two vertex pairs $(r, s), (v, w) \in V(G)^2$ such that (r, s) is contained in C while (v, w) is not and $P_{vw}^K = P_{rs}^K$.

Reverse process: Tau-leaping and Predictor-Corrector At the sampling stage, we use τ -leaping to generate new samples. We first sample the graph size and then sample the noisy graph $G^{(t)}$ from the prior distribution. At each iteration, we keep $G^{(t)}$ and $\hat{R}^{t, \theta}(G, \tilde{G})$ constant and simulate the reverse process for a time interval of τ . In practice, we count all the transitions between t and $t - \tau$ and apply them simultaneously.

The number of transitions between $x_i^{(t)}$ and \tilde{x}_i (respectively $e_{ij}^{(t)}$ and \tilde{e}_{ij}) is Poisson distributed with mean $\tau R_X^{(t), \theta}(x_i^{(t)}, \tilde{x}_i)$ (respectively $\tau \hat{R}_E^{(t), \theta}(e_{ij}^{(t)}, \tilde{e}_{ij})$). Since our state space has no ordinal structure, multiple transitions in one dimension are meaningless, and we reject them. In addition, we experiment using the predictor-corrector scheme. After each predictor step using $\hat{R}^{(t), \theta}(G, \tilde{G})$, we can also apply several corrector steps using the expression defined in Campbell et al. [2022], i.e., $\hat{R}^{(t), c} = \hat{R}^{(t), \theta} + R^{(t)}$.

This rate admits the $q_t(G^{(t)})$ as its stationary distribution, which means that applying the corrector steps brings the distribution of noisy graphs at time t closer to the marginal distribution of the forward process.

Equivariance properties Since graphs are invariant to node reordering, it is essential to design methods that capture this fundamental property of the data. Relying on the similarities between COMETH and DIGRESS, it is straightforward to establish that COMETH is permutation-equivariant and that our loss is permutation-invariant. We also establish that the τ -leaping sampling scheme and the predictor-corrector yield exchangeable distributions, i.e., the model assigns each graph permutation the same probability. Since those results mainly stem from proofs outlined in Vignac et al. [2022], we moved them to appendix A.4.

Conditional generation If unconditional generation is essential to designing an efficient diffusion model, conditioning the generation on some high-level property is critical in numerous real-world applications [Corso et al., 2023, Lee and Min, 2022]. In addition, Vignac et al. [2022] used *classifier guidance*, which relies on a trained unconditional model guided by a regressor on the target property. However, to our knowledge, classifier guidance has yet to be adapted to continuous-time discrete-state diffusion models. We therefore leverage another approach to conditional diffusion model, *classifier-free guidance* [Tang et al., 2022], for which we provide a detailed description in Appendix A.5.

4 Experiments

In the following, we empirically evaluate COMETH on synthetic and real-world graph generation benchmarks.

4.1 Synthetic graph generation: PLANAR and SBM

Datasets & metrics We first validate our method on two benchmarks proposed by Martinkus et al. [2022], PLANAR and SBM. We measure four standard metrics to assess the ability of our model to capture topological properties of the graph distributions, i.e., degree (**Deg.**), clustering coefficient (**Clus.**), count of orbits with four nodes (**Orbit**), and the eigenvalues of the graph Laplacian (**Spec.**). The reported values are the maximum mean discrepancies (MMD) between those metrics evaluated on the generated graphs and the test set. We also report the percentage of valid, unique, and novel (**V.U.N.**) samples among the generated graphs to further assess the ability of our model to capture the properties of the targeted distributions correctly. We provide a detailed description of the metrics in appendix C.1.

Baselines We evaluate our model against several graph diffusion models, namely DIGRESS [Vignac et al., 2022], GRUM [Jo et al., 2024], two autoregressive models, GRAN [Liao et al., 2019], and GRAPHNN [You et al., 2018], and a GAN, SPECTRE [Martinkus et al., 2022].

Results Table 1 gives the results. In contrast to the baselines, we report the average of 5 runs and include error bars. Our experiments revealed that all metrics exhibit high variance across runs, and we thus recommend that future works report error bars to accurately evaluate models on these benchmarks. On PLANAR, our approach yields good results overall metrics, outperforming all the baselines on **V.U.N.** We observe that the sampling quality benefits from the predictor-corrector scheme, with a near-perfect **V.U.N.** score. On SBM, we also obtain SOTA results on all metrics. However, we found that the predictor-corrector did not bring any improvement to this dataset.

4.2 Small molecule generation: QM9

Datasets & metrics To assess the ability of our method to model attributed graph distributions, we evaluate its performance on the standard dataset QM9 (Wu et al. [2018]). Molecules are kekulized using the RDKit library, removing hydrogen atoms. We use the same split as Vignac et al. [2022], with 100k molecules for training, 10k for testing, and the remaining data for the validation set. We want to stress that this split differs from Jo et al. [2022], which uses $\sim 120k$ molecules for training and the rest as a test set. We choose to use the former version of this dataset because it allows for selecting the best checkpoints based on the evaluation of the ELBO on the validation set.

We report the **Validity** over 10k molecules, as evaluated by RDKit sanitization, as well as the **Uniqueness**, **FCD**, using the MOSES benchmark, and **NSPDK**. Appendix C.2 provides a complete description of the metrics.

Table 1: **Synthetic graph generation results.** We report the mean of 5 runs, as well as 95% confidence intervals. Baseline results are taken from Jo et al. [2024], which do not report error bars.

Model	Deg. ↓	Clus. ↓	Orbit ↓	Spec. ↓	V.U.N. [%] ↑
<i>Planar graphs</i>					
GRAPHRNN	24.5	9.0	2508	8.8	0
GRAN	3.5	1.4	1.8	1.4	0
SPECTRE	2.5	2.5	2.4	2.1	25
DiGRESS	1.4	1.2	1.7	-	75
GRUM	2.5	1.1	1.8	1.2	90
COMETH	3.6±1.5	2.0±.2	2.3±1.6	1.4±.1	91.5±4.3
COMETH-PC	2.8±2.3	1.4±.3	3.2±1.2	1.3±.2	99.5±.9
<i>Stochastic block model</i>					
GRAPHRNN	6.9	1.7	3.1	1.0	5
GRAN	14.1	1.7	2.1	0.9	25
SPECTRE	1.9	1.6	1.6	0.9	53
DiGRESS	1.6	1.5	1.7	-	74
GRUM	0.9	1.5	1.8	0.8	85
COMETH	2.5±.4	1.5±.0	1.5±.2	0.9±.1	75±3.7

Table 2: **Molecule generation results on QM9.** We report the mean of 5 runs, as well as 95% confidence intervals. Best results are highlighted in bold. Baseline results are taken from Jang et al. [2023].

Model	Validity ↑	Uniqueness ↑	Valid & Unique ↑	FCD ↓	NSPDK ↓
GDSS	95.72	98.46	94.25	2.9	0.003
DiGRESS	99.01	96.34	95.39	0.25	0.001
GRAPHARM	90.25	95.26	85.97	1.22	0.002
HGGT	99.22	95.65	94.90	0.40	0.000
COMETH	99.57 ±.07	96.76±.17	96.34 ±.2	0.25 ±.01	0.000 ±.000

Baselines We evaluate our model against several recent graph generation models, including two diffusion models, DiGRESS Vignac et al. [2022] and GDSS Jo et al. [2022]), and two autoregressive models, HGGT Jang et al. [2023] and GRAPHARM Kong et al. [2023]).

Results We report results using 500 denoising steps for a fair comparison, as in Vignac et al. [2022]. COMETH performs very well on this simple molecular dataset, notably outperforming its discrete-time counterpart DiGRESS in terms of valid and unique samples with similar FCD and NSPDK. We experimentally found that the predictor-corrector does not improve performance on this dataset; therefore, we do not report results using this sampling scheme.

4.3 Molecule generation on large datasets: MOSES and GuacaMol

Datasets & benchmarks We also evaluate our model on two much larger molecular datasets, MOSES [Polykovskiy et al., 2020]) and GuacaMol [Brown et al., 2019]. The former is a refinement of the ZINC database and includes 1.9M molecules, with 1.6M allocated to training. The latter is derived from the ChEMBL database and comprises 1.4M molecules, from which 1.1M are used for training. We use a preprocessing step similar to Vignac et al. [2022] for the GuacaMol dataset, which filters molecules that cannot be mapped from SMILES to graph and back to SMILES.

Both datasets come with their own metrics and baselines, which we briefly describe here. As for QM9, we report **Validity**, as well as the percentage of **Valid & Unique (Val. & Uni.)** samples, and **Valid, Unique and Novel (V.U.N.)** samples for both datasets. We also report **Filters, FCD, SNN**, and **Scaf** for MOSES, as well as **KL div** and **FCD** for GuacaMol. These metrics are designed to evaluate the model’s capability to capture the chemical properties of the learned distributions. We provide a detailed description of those metrics in appendix C.3.

Results Similarly to previous graph generation models, COMETH does not match the performance of molecule generation methods that incorporate domain-specific knowledge, especially SMILES-based models (Table 3). COMETH further bridges the gap between graph diffusion models and those methods, outperforming DiGRESS in terms of validity by a large margin.

Table 3: **Molecule generation on MOSES.** We report the mean of 5 runs, as well as 95% confidence intervals.

Model	Class	Val. \uparrow	Val. & Uni. \uparrow	V.U.N. \uparrow	Filters \uparrow	FCD \downarrow	SNN \uparrow	Scaf \uparrow
VAE	Smiles	97.7	97.5	67.8	99.7	0.57	0.58	5.9
JT-VAE	Fragment	100	100	99.9	97.8	1.00	0.53	10
GRAPHINVENT	Autoreg.	96.4	96.2	—	95.0	1.22	0.54	12.7
DIGRESS	One-shot	85.7	85.7	81.4	97.1	1.19	0.52	14.8
COMETH	One-shot	87.0 \pm .2	86.9 \pm .2	83.8 \pm .2	97.2 \pm .1	1.44 \pm .02	0.51 \pm .0	15.9 \pm .8
COMETH-PC	One-shot	90.5 \pm .3	90.4 \pm .3	83.7 \pm .2	99.1 \pm .1	1.27 \pm .02	0.54 \pm .0	16.0 \pm .7

Table 4: **Molecule generation on GuacaMol.** We report the mean of 5 runs, as well as 95% confidence intervals. Conversely to MOSES, the GuacaMol benchmark reports scores, so higher is better.

Model	Class	Val. \uparrow	Val. & Uni. \uparrow	V.U.N. \uparrow	KL div \uparrow	FCD \uparrow
LSTM	Smiles	95.9	95.9	87.4	99.1	91.3
NAGVAE	One-shot	92.9	95.5	88.7	38.4	0.9
MCTS	One-shot	100.0	100.0	95.4	82.2	1.5
DIGRESS	One-shot	85.2	85.2	85.1	92.9	68.0
COMETH	One-shot	94.4 \pm .2	94.4 \pm .2	93.5 \pm .3	94.1 \pm .4	67.4 \pm .3
COMETH - PC	One-shot	98.9 \pm .1	98.9 \pm .1	97.6 \pm .2	96.7 \pm .2	72.7 \pm .2

On GuacaMol (Table 4), COMETH obtains excellent performance in terms of V.U.N. samples, with an impressive 12.6% improvement over DIGRESS. However, the LSTM model still outperforms the graph diffusion model on the FCD metric, showcasing a better ability to model the whole distribution.

4.4 Conditional generation

We perform conditional generation on QM9 following the setting of Vignac et al. [2022]. We target two molecular properties, the **dipole moment** μ and the **highest occupied molecular orbital energy (HOMO)**. We sample 100 properties from the test set for each experiment and use them as conditioners to generate 10 molecules. We estimate the properties of the sampled molecules using the Psi4 library (Smith et al. [2020]) and report the **mean absolute error (MAE)** between the estimated properties from the generated set and the targeted properties.

Table 5: **Conditional molecule generation results on QM9.** We report the mean of 5 runs, as well as 95% confidence intervals.

Model	μ		HOMO		μ & HOMO	
	MAE \downarrow	Val \uparrow	MAE \downarrow	Val \uparrow	MAE \downarrow	Val \uparrow
DIGRESS	0.81	—	0.56	—	0.87	—
COMETH	0.67 \pm .02	88.8 \pm .5	0.32 \pm .01	94.1 \pm .8	0.58 \pm .01	92.5 \pm .7

We report our results against DIGRESS in Table 5. Overall, COMETH outperforms DIGRESS by large margin, with 18%, 43%, and 33% improvements on μ , HOMO and both targets respectively. Those performance improvements indicate the superiority of classifier-free guidance over classifier-guidance for conditional graph generation.

5 Conclusion

Here, to leverage the benefits of continuous-time and discrete-state diffusion model, we proposed COMETH, a continuous-time discrete-state graph diffusion model, integrating graph data into a continuous diffusion model framework. We introduced a new noise model adapted to graph specificities using different node and edge rates and a tailored marginal distribution and noise schedule. In addition, we successfully replaced the structural features of DIGRESS with a single encoding with provable expressivity guarantees, removing unnecessary features. Empirically, we showed that integrating continuous time leads to significant improvements across various metrics over state-of-the-art discrete-state diffusion models on a large set of molecular and non-molecular benchmark datasets.

Acknowledgments

This work was performed as part of the Helmholtz School for Data Science in Life, Earth and Energy (HDS-LEE) and received funding from the Helmholtz Association of German Research Centres. Christopher Morris is partially funded by a DFG Emmy Noether grant (468502433) and RWTH Junior Principal Investigator Fellowship under Germany’s Excellence Strategy.

References

- J. Austin, D. D. Johnson, J. Ho, D. Tarlow, and R. Van Den Berg. Structured denoising diffusion models in discrete state-spaces. *Advances in Neural Information Processing Systems*, 34:17981–17993, 2021.
- A. Bergmeister, K. Martinkus, N. Perraudin, and R. Wattenhofer. Efficient and scalable graph generation through iterative local expansion. *arXiv preprint arXiv:2312.11529*, 2023.
- N. Brown, M. Fiscato, M. H. Segler, and A. C. Vaucher. Guacamol: benchmarking models for de novo molecular design. *Journal of chemical information and modeling*, 59(3):1096–1108, 2019.
- A. Campbell, J. Benton, V. De Bortoli, T. Rainforth, G. Deligiannidis, and A. Doucet. A continuous time framework for discrete denoising models. *Advances in Neural Information Processing Systems*, 35:28266–28279, 2022.
- X. Chen, J. He, X. Han, and L.-P. Liu. Efficient and degree-guided graph generation via discrete diffusion modeling. In *International Conference on Machine Learning*, pages 4585–4610, 2023.
- G. Corso, B. Jing, R. Barzilay, T. Jaakkola, et al. Diffdock: Diffusion steps, twists, and turns for molecular docking. In *International Conference on Learning Representations*, 2023.
- G. Cybenko. Approximation by superpositions of a sigmoidal function. *Math. Control. Signals Syst.*, 5(4):455, 1992.
- V. P. Dwivedi, A. T. Luu, T. Laurent, Y. Bengio, and X. Bresson. Graph neural networks with learnable structural and positional representations. In *International Conference on Learning Representations*, 2021.
- M. Fürer. On the combinatorial power of the Weisfeiler-Lehman algorithm. In D. Fotakis, A. Pagourtzis, and V. T. Paschos, editors, *Algorithms and Complexity - 10th International Conference*, 2017.
- K. K. Haefeli, K. Martinkus, N. Perraudin, and R. Wattenhofer. Diffusion models for graphs benefit from discrete state spaces. In *The First Learning on Graphs Conference*, 2022.
- J. Ho and T. Salimans. Classifier-free diffusion guidance. In *NeurIPS 2021 Workshop on Deep Generative Models and Downstream Applications*, 2021.
- J. Ho, A. Jain, and P. Abbeel. Denoising diffusion probabilistic models. In *Advances in Neural Information Processing Systems*, 2020.
- E. Hoogeboom, D. Nielsen, P. Jaini, P. Forré, and M. Welling. Argmax flows and multinomial diffusion: Learning categorical distributions. *Advances in Neural Information Processing Systems*, 34:12454–12465, 2021.
- C. Hua, S. Luan, M. Xu, Z. Ying, J. Fu, S. Ermon, and D. Precup. Mudiff: Unified diffusion for complete molecule generation. In *Learning on Graphs Conference*, 2024.
- Y. Huang, W. Lu, J. Robinson, Y. Yang, M. Zhang, S. Jegelka, and P. Li. On the stability of expressive positional encodings for graph neural networks. In *International Conference on Learning Representations*, 2023.
- I. Igashov, A. Schneuing, M. Segler, M. M. Bronstein, and B. Correia. Retrobridge: Modeling retrosynthesis with markov bridges. In *International Conference on Learning Representations*, 2023.
- Y. Jang, D. Kim, and S. Ahn. Graph generation with K^2 -trees. In *The Twelfth International Conference on Learning Representations*, 2023.

- J. Jo, S. Lee, and S. J. Hwang. Score-based generative modeling of graphs via the system of stochastic differential equations. In *International Conference on Machine Learning*, pages 10362–10383, 2022.
- J. Jo, D. Kim, and S. J. Hwang. Graph generation with diffusion mixture. *arXiv preprint arXiv:2302.03596*, 2024.
- L. Kong, J. Cui, H. Sun, Y. Zhuang, B. A. Prakash, and C. Zhang. Autoregressive diffusion model for graph generation. In *International Conference on Machine Learning*, pages 17391–17408, 2023.
- D. Kreuzer, D. Beaini, W. Hamilton, V. Létourneau, and P. Tossou. Rethinking graph transformers with spectral attention. *Advances in Neural Information Processing Systems*, pages 21618–21629, 2021.
- T. Le, J. Cremer, F. Noe, D.-A. Clevert, and K. T. Schütt. Navigating the design space of equivariant diffusion-based generative models for de novo 3d molecule generation. In *International Conference on Learning Representations*, 2023.
- M. Lee and K. Min. Mgcvae: multi-objective inverse design via molecular graph conditional variational autoencoder. *Journal of chemical information and modeling*, 62(12):2943–2950, 2022.
- M. Leshno, V. Y. Lin, A. Pinkus, and S. Schocken. Multilayer feedforward networks with a non-polynomial activation function can approximate any function. *Neural Networks*, 6(6):861–867, 1993.
- R. Liao, Y. Li, Y. Song, S. Wang, W. Hamilton, D. K. Duvenaud, R. Urtasun, and R. Zemel. Efficient graph generation with graph recurrent attention networks. *Advances in Neural Information Processing Systems*, 2019.
- D. Lim, J. D. Robinson, L. Zhao, T. E. Smidt, S. Sra, H. Maron, and S. Jegelka. Sign and basis invariant networks for spectral graph representation learning. *International Conference on Learning Representations (ICLR)*, 2023.
- T. Luo, Z. Mo, and S. J. Pan. Fast graph generation via spectral diffusion. *IEEE Transactions on Pattern Analysis and Machine Intelligence*, 2023.
- L. Ma, C. Lin, D. Lim, A. Romero-Soriano, P. K. Dokania, M. Coates, P. Torr, and S.-N. Lim. Graph inductive biases in transformers without message passing. *arXiv preprint arXiv:2305.17589*, 2023.
- K. Martinkus, A. Loukas, N. Perraudin, and R. Wattenhofer. Spectre: Spectral conditioning helps to overcome the expressivity limits of one-shot graph generators. In *International Conference on Machine Learning*, pages 15159–15179. PMLR, 2022.
- A. Q. Nichol and P. Dhariwal. Improved denoising diffusion probabilistic models. In *International Conference on Machine Learning*, pages 8162–8171, 2021.
- M. Ninniri, M. Podda, and D. Bacciu. Classifier-free graph diffusion for molecular property targeting. *arXiv preprint arXiv:2312.17397*, 2023.
- C. Niu, Y. Song, J. Song, S. Zhao, A. Grover, and S. Ermon. Permutation invariant graph generation via score-based generative modeling. In *International Conference on Artificial Intelligence and Statistics*, pages 4474–4484. PMLR, 2020.
- D. Polykovskiy, A. Zhebrak, B. Sanchez-Lengeling, S. Golovanov, O. Tatanov, S. Belyaev, R. Kurbanov, A. Artamonov, V. Aladinskiy, M. Veselov, et al. Molecular sets (moses): a benchmarking platform for molecular generation models. *Frontiers in pharmacology*, 11:565644, 2020.
- K. Preuer, P. Renz, T. Unterthiner, S. Hochreiter, and G. Klambauer. Fréchet chemnet distance: a metric for generative models for molecules in drug discovery. *Journal of chemical information and modeling*, 58(9):1736–1741, 2018.
- Y. Qin, C. Vignac, and P. Frossard. Sparse training of discrete diffusion models for graph generation. *arXiv preprint arXiv:2311.02142*, 2023.
- G. Rattan and T. Seppelt. Weisfeiler–leman and graph spectra. In *Symposium on Discrete Algorithms*, pages 2268–2285, 2023.

- M. A. Shabani, S. Hosseini, and Y. Furukawa. Housediffusion: Vector floorplan generation via a diffusion model with discrete and continuous denoising. In *IEEE/CVF Conference on Computer Vision and Pattern Recognition*, pages 5466–5475, 2023.
- C. Shi, M. Xu, Z. Zhu, W. Zhang, M. Zhang, and J. Tang. GraphAF: a flow-based autoregressive model for molecular graph generation. In *International Conference on Learning Representations*, 2019.
- D. G. Smith, L. A. Burns, A. C. Simmonett, R. M. Parrish, M. C. Schieber, R. Galvelis, P. Kraus, H. Kruse, R. Di Remigio, A. Alenaizan, et al. Psi4 1.4: Open-source software for high-throughput quantum chemistry. *The Journal of Chemical Physics*, 152(18), 2020.
- J. Sohl-Dickstein, E. Weiss, N. Maheswaranathan, and S. Ganguli. Deep unsupervised learning using nonequilibrium thermodynamics. In *International Conference on Machine Learning*, pages 2256–2265, 2015.
- Y. Song, J. Sohl-Dickstein, D. P. Kingma, A. Kumar, S. Ermon, and B. Poole. Score-based generative modeling through stochastic differential equations. In *International Conference on Learning Representations*, 2020.
- H. Sun, L. Yu, B. Dai, D. Schuurmans, and H. Dai. Score-based continuous-time discrete diffusion models. *arXiv preprint arXiv:2211.16750*, 2022.
- Z. Tang, S. Gu, J. Bao, D. Chen, and F. Wen. Improved vector quantized diffusion models. *arXiv preprint arXiv:2205.16007*, 2022.
- C. Vignac, I. Krawczuk, A. Siraudin, B. Wang, V. Cevher, and P. Frossard. DiGress: Discrete denoising diffusion for graph generation. In *International Conference on Learning Representations*, 2022.
- C. Vignac, N. Osman, L. Toni, and P. Frossard. Midi: Mixed graph and 3d denoising diffusion for molecule generation. In *ICLR 2023-Machine Learning for Drug Discovery workshop*, 2023.
- Z. Wu, B. Ramsundar, E. N. Feinberg, J. Gomes, C. Geniesse, A. S. Pappu, K. Leswing, and V. Pande. Moleculenet: a benchmark for molecular machine learning. *Chemical science*, 9(2):513–530, 2018.
- L. Yang, Z. Zhang, Y. Song, S. Hong, R. Xu, Y. Zhao, W. Zhang, B. Cui, and M.-H. Yang. Diffusion models: A comprehensive survey of methods and applications. *ACM Computing Surveys*, 56(4):1–39, 2023.
- J. Yim, B. L. Trippe, V. De Bortoli, E. Mathieu, A. Doucet, R. Barzilay, and T. Jaakkola. xarxiv preprint arxiv:2305.17589generation. In *International Conference on Machine Learning*, pages 40001–40039, 2023.
- J. You, R. Ying, X. Ren, W. Hamilton, and J. Leskovec. GraphRNN: Generating realistic graphs with deep auto-regressive models. In *International Conference on Machine Learning*, pages 5708–5717, 2018.

Appendices

We provide proofs and additional theoretical background in appendix A. We give details on our implementation in appendix B and experimental details in appendix C. Finally, we provide visualization for generated samples in appendix E.

A Theoretical details

Here, we outline the theoretical details of our COMETH architecture.

A.1 Additional background

Notation Let $\mathbb{N} := \{1, 2, 3, \dots\}$. For $m \geq 1$ and $n \geq m$, let $\llbracket m, n \rrbracket := \{m, \dots, n\} \subset \mathbb{N}$. We denote the *forward diffusion kernel* by $q(z^{(t)} | z^{(t-1)})$, i.e., the probability of transitioning between a state at time $t - 1$ and t . We superscript t to denote the noisy state at time t . In discrete time, we have $t \in \llbracket 0, T \rrbracket$. Given a state $z^{(t)} \in \mathcal{Z}$, the vector $z^{(t)}$ denotes its one-hot encoding. Further, we denote $p^\theta(z^{(t-1)} | z^{(t)})$ the model for the *reverse transitions* and by $p^\theta(z^{(0)} | z^{(t)})$ the neural network with parameters θ .

Discrete diffusion In the discrete case, we aim at modeling the probability $p_{\text{data}}(z_0)$ of sampling z_0 . Thereto, we define a *forward Markov process* that gradually transforms the data distribution into a well-known, easy-to-sample target distribution p_{ref} . This is done by defining a *sequence of forward kernels* $q(z^{(t)} | z^{(t-1)})$, such that after t steps the joint distribution of the trajectory is $q(z^{(t)} | z^{(0)}) = \prod_{i=1}^t q(z^{(i)} | z^{(i-1)})$. We typically want the forward process to mix quickly towards p_{ref} and to have a closed-form expression for efficient training. The reverse process is also Markovian, and its transition kernel can be derived using Bayes' rule, i.e.,

$$q(z^{(t-1)} | z^{(t)}) := \frac{q(z^{(t)} | z^{(t-1)})q(z^{(t-1)})}{q(z^{(t)})}.$$

However, in practice, evaluating the above is intractable. Hence, we learn reverse transitions through a parametric approximation $p^\theta(z^{(t-1)} | z^{(t)})$, which is defined via the expression of $q(z^{(t-1)} | z^{(t)})$ and the *denoising neural network* $p^\theta(z^{(0)} | z^{(t)})$, where

$$p^\theta(z^{(t-1)} | z^{(t)}) := q(z^{(t)} | z^{(t-1)}) \sum_{z^{(0)}} \frac{q(z^{(t-1)} | z^{(0)})}{q(z^{(t)} | z^{(0)})} p^\theta(z^{(0)} | z^{(t)}).$$

The denoising neural network is optimized by minimizing the evidence lower bound (ELBO) [Sohl-Dickstein et al., 2015]. During sampling, noise is sampled from p_{ref} , and a new sample is created by performing the reverse transitions using $p^\theta(z^{(t-1)} | z^{(t)})$.

In practice, the noise model of a discrete diffusion model is a sequence of $S \times S$ transition matrices $(\mathbf{Q}^{(1)}, \dots, \mathbf{Q}^{(T)})$ such that $[\mathbf{Q}^{(t)}]_{ij}$ represents the probability of transitioning from state i to state j at time step t , i.e., $q(z^{(t)} | z^{(t-1)}) := z^{(t-1)} \mathbf{Q}^{(t)}$. A simple example of a transition matrix is the uniform transition matrix $\mathbf{Q}^{(t)} := \alpha^{(t)} \mathbf{I} + (1 - \alpha^{(t)}) \mathbf{1}\mathbf{1}'/S$, with $\alpha^{(t)}$ transitioning from 1 to 0 [Austin et al., 2021], Hooeboom et al. [2021]. In the case of graphs, Vignac et al. [2022] proposed a transition matrix in which the probability of transition for a given class depends on its frequency in the dataset.

Continuous-time discrete diffusion Here, we provide additional details on how to properly design the rate matrix $\mathbf{R}^{(t)}$ to allow efficient optimization. Recall the definition of the forward process,

$$q_{t+\Delta t|t}(\tilde{z} | z^{(t)}) := \delta_{\tilde{z}, z^{(t)}} + \mathbf{R}^{(t)}(z^{(t)}, \tilde{z}) \Delta t,$$

with $\delta_{\tilde{z}, z^{(t)}} = 1$ if $\tilde{z} = z^{(t)}$, and 0 else. The rate matrix should respect the following requirements,

$$R^{(t)}(z^{(t)}, \tilde{z}) \geq 0, \quad \text{and} \quad R^{(t)}(z^{(t)}, z^{(t)}) = - \sum_{\tilde{z}} R^{(t)}(z^{(t)}, \tilde{z}) < 0.$$

Here, the second requirements ensures that $q_{t+\delta t|t}(\cdot | z^{(t)})$ sums to 1.

For efficient optimization of the forward process, the transition matrix $\mathbf{R}^{(t)}$ needs to be conveniently designed. Campbell et al. [2022] established that, when $\mathbf{R}^{(t)}$ and $\mathbf{R}^{(t')}$ commute whatever t and t' , a transition probability matrix can be written as

$$\bar{\mathbf{Q}}^{(t)} = \exp \left(\int_0^t \mathbf{R}^{(s)} ds \right).$$

The above condition is met when the rate is written as $\mathbf{R}^{(t)} = \beta(t)\mathbf{R}_b$, when β is a time-dependent scalar and \mathbf{R}_b is a constant base rate matrix.

A.2 Noise schedule

Proposition 7. For a CTMC $(z^{(t)})_{t \in [0,1]}$ with rate matrix $\mathbf{R}^{(t)} = \beta(t)\mathbf{R}_b$ and $\mathbf{R}_b = \mathbb{1}\mathbf{m}' - \mathbf{I}$, the forward process can be written as

$$\bar{\mathbf{Q}}^{(t)} = e^{-\bar{\beta}^t} \mathbf{I} + (1 - e^{-\bar{\beta}^t}) \mathbb{1}\mathbf{m}',$$

where $(\bar{\mathbf{Q}}^{(t)})_{ij} = q(z^{(t)} = i \mid z^0 = j)$ and $\bar{\beta}^t = \int_0^t \beta(s) ds$.

Proof. Since $\mathbb{1}\mathbf{m}'$ is a rank-one matrix with trace 1, it is diagonalizable and has only one non-zero eigenvalue, equal to $\text{tr}(\mathbb{1}\mathbf{m}') = 1$. Therefore,

$$\mathbf{R}_b = \mathbb{1}\mathbf{m}' - \mathbf{I} = \mathbf{P}\mathbf{D}\mathbf{P}^{-1} - \mathbf{I} = \mathbf{P}(\mathbf{D} - \mathbf{I})\mathbf{P}^{-1},$$

with $\mathbf{D} = \text{diag}(1, 0, \dots, 0)$. Denoting $\bar{\beta}^t = \int_0^t \beta(s) ds$,

$$\begin{aligned} \bar{\mathbf{Q}}^{(t)} &= \mathbf{P} \exp(\bar{\beta}^t(\mathbf{D} - \mathbf{I})) \mathbf{P}^{-1} \\ &= \mathbf{P} \left(\mathbf{D} - e^{-\bar{\beta}^t} \mathbf{I} - e^{-\bar{\beta}^t} \mathbf{D} \right) \mathbf{P}^{-1} \\ &= e^{-\bar{\beta}^t} \mathbf{I} + (1 - e^{-\bar{\beta}^t}) \mathbb{1}\mathbf{m}'. \end{aligned}$$

□

A.3 RRWP properties

Graphs notations A graph G is a pair $(V(G), E(G))$ with *finite* sets of *vertices* or *nodes* $V(G)$ and *edges* $E(G) \subseteq \{\{u, v\} \subseteq V(G) \mid u \neq v\}$. If not otherwise stated, we set $n := |V(G)|$, and the graph is of *order* n . For ease of notation, we denote the edge $\{u, v\} \in E(G)$ by (u, v) or (v, u) . An n -order attributed graph is a pair $\mathbf{G} = (G, \mathbf{X}, \mathbf{E})$, where $G = (V(G), E(G))$ is a graph and $\mathbf{X} \in \mathbb{R}^{n \times a}$, for $a > 0$, is a *node feature matrix* and $\mathbf{E} \in \mathbb{R}^{n \times n \times b}$, for $b > 0$, is an *edge feature tensor*. Here, we set $V(G) := \llbracket 1, n \rrbracket$. The *neighborhood* of $v \in V(G)$ is denoted by $N(v) := \{u \in V(G) \mid (v, u) \in E(G)\}$.

In our experiments, we leverage the *relative random-walk probabilities* (RRWP) encoding, introduced in Ma et al. [2023]. Denoting \mathbf{A} the adjacency matrix of a graph G , and \mathbf{D} the diagonal degree matrix, and $\mathbf{M} = \mathbf{D}^{-1}\mathbf{A}$ the degree-normalized adjacency matrix, for each pair of nodes (i, j) , the RRWP encoding computes

$$P_{ij}^K := [I_{ij}, M_{ij}, M_{ij}^2, \dots, M_{ij}^{K-1}], \quad (3)$$

where K refers to the maximum length of the random walks. The entry P_{ii}^K corresponds to the RWSE encoding of node i ; therefore, we leverage them as node encodings. This encoding alone is sufficient to train our graph diffusion model and attain state-of-the-art results.

In the following, we show that RWPP encoding can (approximately) determine if two nodes lie in the same connected components and approximate the size of the largest connected component.

Proposition 8. For $n \in \mathbb{N}$, let \mathcal{G}_n denote the set of n -order graphs and for a graph $G \in \mathcal{G}_n$ let $V(G) := \llbracket 1, n \rrbracket$. Assume that the graph G has c connected components and let $\mathbf{C} \in \{0, 1\}^{n \times c}$ be a matrix such the i th row \mathbf{C}_i is a one-hot encoding indicating which of the c connected components the vertex i belongs to. Then, for any $\varepsilon > 0$, there exists a feed-forward neural network $\text{FNN}: \mathbb{R}^{n \times n} \rightarrow [0, 1]^{n \times c}$ such that

$$\|\text{FNN}(\mathbf{M}^{n-1}) - \mathbf{C}\|_F \leq \varepsilon.$$

Proof. Let $\mathbf{R} := \mathbf{M}^{n-1}$. First, since the graphs have n vertices, the longest path in the graphs has length $n - 1$. Hence, two vertices $v, w \in V(G)$, with $v \neq w$ are in the same connected component if, and only, if $R_{vw} \neq 0$. Hence, applying a sign activation function to \mathbf{R} pointwisely, we get a matrix over $\{0, 1\}$ with the same property. Further, by adding $\mathbf{D}_n \in \{0, 1\}^{n \times n}$, an $n \times n$ diagonal matrix with ones on the main diagonal, to this matrix, this property also holds for the case of $v = w$. In addition, there exists a permutation matrix \mathbf{P}_n such that applying it to the above matrix results in a block-diagonal matrix $\mathbf{B} \in \{0, 1\}^{n \times n}$ such that $\mathbf{B}_{v \cdot} = \mathbf{B}_{w \cdot}$, for $v, w \in V(G)$, if, and only, if the vertices v, w are in the same connected component. Since n is finite, the number of such \mathbf{B} matrices is finite. Hence, we can find a continuous function mapping each possible row of $\mathbf{B}_{v \cdot}$, for $v \in V(G)$, to the corresponding one-hot encoding of the connected component. Since all functions after applying the sign function are continuous, we can approximate the above composition of functions via a two-layer feed-forward neural network leveraging the universal approximation theorem [Cybenko, 1992, Leshno et al., 1993]. \square

Similarly, we can also approximate the size of the largest component in a given graph.

Proposition 9. For $n \in \mathbb{N}$, let \mathcal{G}_n denote the set of n -order graphs and for $G \in \mathcal{G}_n$ let $V(G) := \llbracket 1, n \rrbracket$. Assume that S is the number of vertices in the largest connected component of the graph G . Then, for any $\varepsilon > 0$, there exists a feed-forward neural network $\text{FNN}: \mathbb{R}^{n \times n} \rightarrow [1, n]$,

$$|\text{FNN}(\mathbf{M}^{n-1}) - S| \leq \varepsilon.$$

Proof. By the proof of Proposition 8, we get a block-diagonal matrix $\mathbf{B} \in \{0, 1\}^{n \times n}$, such that $B_{uv} = 1$ if, and only, if u, v are in the same connected components. Hence, by column-wise summation, we get the number of vertices in each connected component. Hence, there is an $n \times 1$ matrix over $\{0, 1\}$, extracting the largest entry. Since all of the above functions are continuous, we can approximate the above composition of functions via a two-layer feed-forward neural network leveraging the universal approximation theorem [Cybenko, 1992, Leshno et al., 1993]. \square

Moreover, we can show RRWP encodings can (approximately) count the number p -cycles, for $p < 5$, in which a node is contained. A p -cycle is a cycle on p vertices.

Proposition 10. For $n \in \mathbb{N}$, let \mathcal{G}_n denote the set of n -order graphs and for $G \in \mathcal{G}_n$ let $V(G) := \llbracket 1, n \rrbracket$. Assume that $\mathbf{c} \in \mathbb{R}^n$ contains the number of p -cycles a node is contained in for all vertices in G , for $p \in \{3, 4\}$. Then, for any $\varepsilon > 0$, there exists a feed-forward neural network $\text{FNN}: \mathbb{R}^{n \times n} \rightarrow \mathbb{R}^n$,

$$\|\text{FNN}(\mathbf{P}^{n-1}) - \mathbf{c}\|_2 \leq \varepsilon.$$

Proof. For $p \in \{3, 4\}$, Vignac et al. [2022, Appendix B.2] provide simple linear-algebraic equations for the number of p -cycles each vertex of a given graph is contained based on powers of the adjacency matrix, which can be expressed as compositions of linear mappings, i.e., continuous functions. Observe that we can extract these matrices from \mathbf{P}^{n-1} . Further, note that the domain of these mappings is compact. Hence, we can approximate this composition of functions via a two-layer feed-forward neural network leveraging the universal approximation theorem [Cybenko, 1992, Leshno et al., 1993]. \square

However, we can also show that RRWP encodings cannot detect if a node is contained in a large cycle of a given graph. We say that an encoding, e.g., RRWP, counts the number of p -cycles for $p \geq 2$ if there do not exist two graphs, one containing at least one p -cycle while the other does not, while the RRWP encodings of the two graphs are equivalent.

Proposition 11. For $p \geq 8$, the RRWP encoding does not count the number of p -cycles.

Proof. First, by Rattan and Seppelt [2023], the RRWP encoding does not distinguish more pairs of non-isomorphic graphs than the so-called $(1, 1)$ -dimensional Weisfeiler–Leman algorithm. Secondly, the latter algorithm is strictly weaker than the 3-dimensional Weisfeiler–Leman algorithm in distinguishing non-isomorphic graphs [Rattan and Seppelt, 2023, Theorem 1.4]. However, by Fürer [2017, Theorem 4], the 3-dimensional Weisfeiler–Leman algorithm cannot count 8-cycles. \square

Hence, the above proposition implies the following results.

Corollary 12. For $p \geq 8$ and $K \geq 0$, there exists a graph G containing a p -cycle C , and two vertex pairs $(r, s), (v, w) \in V(G)^2$ such that (r, s) is contained in C while (v, w) is not and $P_{vw}^K = P_{rs}^K$.

A.4 Equivariance properties

In this section, we prove that our model is equivariant (Proposition 13) and that our loss is permutation-invariant (Proposition 14), relying on Vignac et al. [2022, Lemma 3.1 and 3.2]. We also prove exchangeability with Proposition 15.

Let us start by defining the notation for a *graph permutation*. Denote π a permutation, π acts on the attributed graph $G = (G, \mathbf{X}, \mathbf{E})$ as,

- $\pi G = (V(\pi G), E(\pi G))$ where $V(\pi G) = \{\pi(1), \dots, \pi(n)\}$ and $E(\pi G) = \{(\pi(i), \pi(j)) \mid (v_i, v_j) \in E(G)\}$,
- $\pi \mathbf{X}$ the matrix obtained by permutating the rows of \mathbf{X} according to π , i.e. $(\pi \mathbf{X})_i = \mathbf{x}_{\pi^{-1}(i)}$,
- Similarly, $\pi \mathbf{E}$ is the tensor obtained by the permutation of the components e_{ij} of \mathbf{E} according to π , i.e. $(\pi \mathbf{E})_{ij} = e_{\pi^{-1}(i)\pi^{-1}(j)}$.

Proposition 13 (Equivariance). DIGRESS' graph transformer using RWSE as node encodings and RRWP as edge encodings is permutation equivariant.

Proof. We recall the sufficient three conditions stated in Vignac et al. [2022] for ensuring permutation-equivariance of the DIGRESS architecture, namely,

- their set of structural and spectral features is equivariant.
- All the blocks of their graph transformer architecture are permutation equivariant.
- The layer normalization is equivariant.

Replacing the first condition with the permutation-equivariant nature of the RRWP-based node and edge encodings completes the proof. \square

We now derive a more thorough proof of the permutation invariance of the loss compared to Vignac et al. [2022, Lemma 3.2], relying on the permutation-equivariant nature of both the forward process and the denoising neural network.

Proposition 14 (Permutation invariance of the loss). The cross-entropy loss defined in Equation 1 is invariant to the permutation of the input graph $G^{(0)}$.

Proof. Given a graph $G = (G, \mathbf{X}, \mathbf{E})$, we denote by $\hat{G} = (\hat{G}, \hat{\mathbf{X}}, \hat{\mathbf{E}})$ the predicted clean graph by the neural network and $\pi G = (\pi G, \pi \mathbf{X}, \pi \mathbf{E})$ a permutation of this graph, for arbitrary permutation π . Let us now establish that the loss function is permutation-invariant. We recall the loss function for a permutation π of the clean data sample $G^{(0)}$ is

$$\mathcal{L}_{\text{CE}} := \mathbb{E}_{t \sim [0,1], p_{\text{data}}(\pi G^{(0)}), q(\pi G^{(t)} | \pi G^{(0)})} \left[- \sum_i^n \log p_{0|t}^\theta(x_{\pi(i)}^{(0)} | \pi G^{(t)}) - \lambda \sum_{i < j}^n \log p_{0|t}^\theta(e_{\pi(i)\pi(j)}^{(0)} | \pi G^{(t)}) \right].$$

Because dimensions are noised independently, the true data distribution $p_{\text{data}}(\pi G^{(0)}) = p_{\text{data}}(G^{(0)})$ is permutation-invariant, and the forward process is permutation-equivariant. Thus, we can write,

$$\mathcal{L}_{\text{CE}} := \mathbb{E}_{t \sim [0,1], p_{\text{data}}(G^{(0)}), q(G^{(t)} | G^{(0)})} \left[- \sum_i^n \log p_{0|t}^\theta(x_{\pi(i)}^{(0)} | \pi G^{(t)}) - \lambda \sum_{i < j}^n \log p_{0|t}^\theta(e_{\pi(i)\pi(j)}^{(0)} | \pi G^{(t)}) \right].$$

Using Proposition 13, we also have that $p_{0|t}^\theta(x_i^{(0)} | G^{(t)}) = p_{0|t}^\theta(x_{\pi(i)}^{(0)} | \pi G^{(t)})$ and $p_{0|t}^\theta(e_{ij}^{(0)} | G^{(t)}) = p_{0|t}^\theta(e_{\pi(i)\pi(j)}^{(0)} | \pi G^{(t)})$, which concludes the proof. \square

Proposition 14 shows that, whatever permutation of the original graph we consider, the loss function remains the same, and so do the gradients. Hence, we do not have to consider all the permutations of the same graph during the optimization process.

Proposition 15 (Exchangeability). COMETH yields exchangeable distributions.

Proof. To establish the exchangeability, we require two conditions, a permutation-invariant prior distribution and an equivariant reverse process.

- Since nodes and edges are sampled i.i.d from the same distribution, our prior distribution is permutation-invariant, i.e., each permutation of the same random graph has the same probability of being sampled. Hence $p_{\text{ref}}(\pi G^{(T)}) = p_{\text{ref}}(G^{(T)})$.
- It is straightforward to see that our reverse rate is permutation-equivariant regarding the joint permutations of $G^{(t)}$ and $G^{(0)}$. We illustrate this using the node reverse rate,

$$R_X^t(\tilde{x}_i, x_i^{(t)}) \sum_{x_0} \frac{q_{t|0}(\tilde{x}_i | x_i^{(0)})}{q_{t|0}(x_i^{(t)} | x_i^{(0)})} p_{0|t}^\theta(x_i^{(0)} | \mathbf{G}^{(t)}).$$

The forward rate, as well as the forward process, is permutation-equivariant regarding the joint any permutation on $G^{(t)}$ and $G^{(0)}$, and the neural network is permutation-equivariant. Similarly, we can reason regarding the edge reverse rate. Therefore, the overall reverse rate is permutation-equivariant. Since we sample independently across dimensions, the τ -leaping procedure is also permutation-equivariant. □

A.5 Classifier-free guidance

In the conditional generation setting, one wants to generate samples satisfying a specific property \mathbf{y} , to which we refer as *the conditioner*. For example, in text-to-image diffusion models, the conditioner consists of a textual description specifying the image the model is intended to generate. The most straightforward way to perform conditional generation for diffusion models is to inject the conditioner into the network—therefore modeling $p^\theta(z^{(t-1)} | z^{(t)}, \mathbf{y})$ —hoping that the model will take it into account. However, the network might ignore \mathbf{y} , and several efficient approaches to conditional generation for diffusion models were consequently developed.

The approach leveraged by Vignac et al. [2022] to perform conditional generation is classifier-guidance. It relies on a trained unconditional diffusion model and a regressor, or classifier, depending on the conditioner, trained to predict the conditioner given noisy inputs. As mentioned in Ho and Salimans [2021], it has the disadvantage of complicating the training pipeline, as a pre-trained classifier cannot be used during inference.

To avoid training a classifier to guide the sampling process, *classifier-free guidance* has been proposed in Ho and Salimans [2021] and then adapted for discrete data in Tang et al. [2022]. A classifier-free conditional diffusion model jointly trains a conditional and unconditional model through *conditional dropout*. That is, the conditioner is randomly dropped with probability p_{uncond} during training, in which the conditioner is set to a null vector. However, Tang et al. [2022] showed that learning the null conditioner jointly with the model’s parameters is more efficient.

At the sampling stage, the next state is sampled through

$$\log p^\theta(z^{(t-1)} | z^{(t)}, \mathbf{y}) = \log p^\theta(z^{(t-1)} | z^{(t)}, \emptyset) + (s+1)(\log p^\theta(z^{(t-1)} | z^{(t)}, \mathbf{y}) - \log p^\theta(z^{(t-1)} | z^{(t)}, \emptyset)), \quad (4)$$

where s is the *guidance strength*. We refer to Tang et al. [2022] for deriving the above expression for the sampling process.

Let us now explain how we apply classifier-free guidance in our setting. Denoting $\hat{R}^{t,\theta}(\mathbf{G}, \tilde{\mathbf{G}} | \mathbf{y})$, the conditional reverse rate can be written as

$$\hat{R}^{t,\theta}(\mathbf{G}, \tilde{\mathbf{G}} | \mathbf{y}) = \sum_i \delta_{\mathbf{G} \setminus x_i, \tilde{\mathbf{G}} \setminus x_i} \hat{R}_X^{t,\theta}(x_i^{(t)}, \tilde{x} | \mathbf{y}) + \sum_{i < j} \delta_{\mathbf{G} \setminus e_{ij}, \tilde{\mathbf{G}} \setminus e_{ij}} \hat{R}_E^{t,\theta}(e_{ij}^{(t)}, \tilde{e}_{ij} | \mathbf{y}),$$

and

$$\hat{R}_X^{t,\theta}(x_i^{(t)}, \tilde{x}) = R_X^t(\tilde{x}_i, x_i^{(t)}) \sum_{x_0} \frac{q_{t|0}(\tilde{x}_i | x_i^{(0)})}{q_{t|0}(x_i^{(t)} | x_i^{(0)})} p_{0|t}^\theta(x_i^{(0)} | \mathbf{G}^{(t)}, \mathbf{y}), \text{ for } x_i^{(t)} \neq \tilde{x}_i,$$

and similarly for edges. At the sampling stage, we first compute the unconditional probability distribution $p_{0|t}^\theta(x_i^{(0)} | \mathbf{G}^{(t)}, \emptyset)$, where \emptyset denotes the learned null vector, then the conditional distribution

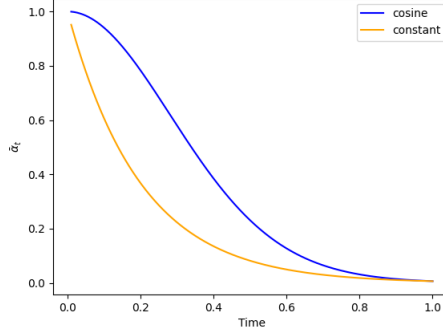


Figure 2: Comparison between our cosine noise schedule and the constant noise schedule proposed by Campbell et al. [2022]. Both schedules are plotted using a rate constant $\alpha = 5$.

$p_{0|t}^\theta(x_i^{(0)} | \mathbf{G}^{(t)}, \mathbf{y})$. These two distributions are combined in the log-probability space in the following way,

$$\log p^\theta(z^{(t-1)} | z^{(t)}, \mathbf{y}) = \log p^\theta(z^{(t-1)} | z^{(t)}, \emptyset) + (s+1)(\log p^\theta(z^{(t-1)} | z^{(t)}, \mathbf{y}) - \log p^\theta(z^{(t-1)} | z^{(t)}, \emptyset)). \quad (5)$$

Finally, the distribution in Equation (5) is exponentiated and plugged into the reverse rate.

B Implementation details

Here, we provide some implementation details.

B.1 Noise schedule

We plot our noise schedule against the constant noise schedule used for categorical data in Campbell et al. [2022] in Figure 2. Following Proposition 1, we plot $\bar{\alpha}_t = e^{-\bar{\beta}_t}$ on the y -axis, quantifying the information level of the original data sample retained at time t . Similarly to Nichol and Dhariwal [2021], we can see that the constant noise schedule converges towards zero faster than the cosine schedule, hence degrading the data faster.

In our experiments, we perform a hyperparameter search to select the best rate constant for each dataset, with $\alpha \in \{4, 5, 6\}$.

Following Campbell et al. [2022]; we set a minimum time to $t_{\min} = 0.01T$ because the reverse rates are ill-conditioned close to $t = 0$.

B.2 Algorithms

We provide the pseudo-code for the training and sampling from COMETH in Figure 3. Similar to Campbell et al. [2022], we apply a last neural network pass at $t = t_{\min}$ and take the node and edge types to the types with the highest predicted probability.

We omit the corrector steps in the sampling algorithm for conciseness. They are exactly the same than the predictor τ -leaping steps, using the corrector rate $\hat{R}^{(t),c} = \hat{R}^{(t),\theta} + R^{(t)}$, and applied after time update, i.e. at $t = \tau$. Since those steps are sampled from different CTMC with rate $\hat{R}^{(t),c}$, we have control over τ when applying corrector steps. We provide additional details on the choice of this hyperparameter, denoted as τ_c , in appendix C.

B.3 Graph transformer

See Figure 4 for an overview of the used graph transformer, building on Vignac et al. [2022].

Algorithm 1: Training

Input: A graph $G = (X, E)$
Sample $t \sim \mathcal{U}([0, 1])$
Sample $G^t \sim \mathbf{X} \hat{Q}_X^t \times \mathbf{E} \hat{Q}_E^t$ ▷ Sample sparse noisy graph
Predict $p_{0|t}^\theta(G | G^t)$ ▷ Predict clean graph using neural network
 $\mathcal{L}_{CE} \leftarrow -\sum_i \log p_{0|t}^\theta(x_i^{(0)} | G^t) - \lambda \sum_{i < j} \log p_{0|t}^\theta(e_{ij}^{(0)} | G^t)$
Update θ using \mathcal{L}_{CE}

Algorithm 2: τ -leaping sampling from Cometh

Sample n from the training data distribution
Sample $G^{(T)} \sim \prod_i m_X \prod_{ij} m_E$ ▷ Sample random graph from prior distribution
while $t > 0.01$ **do**
 for $i = 1$ **to** n **do**
 for \tilde{x} in \mathcal{X} **do**
 $\hat{R}_X^{t,\theta}(x_i^{(t)}, \tilde{x}) = R_X^t(\tilde{x}_i, x_i^{(t)}) \sum_{x_0} \frac{q_{t|0}(\tilde{x}_i | x_i^{(0)})}{q_{t|0}(x_i^{(t)} | x_i^{(0)})} p_{0|t}^\theta(x_i^{(0)} | G^t)$, for $x_i^{(t)} \neq \tilde{x}_i$
 Sample $j_{x_i^{(t)}, \tilde{x}} \sim \mathcal{P}(\tau \hat{R}_X^{t,\theta}(x_i^{(t)}, \tilde{x}))$ ▷ Count transitions on node i
 end
 end
 for $i, j = 1$ **to** n , $i < j$ **do**
 for \tilde{e} in \mathcal{E} **do**
 $\hat{R}_E^{t,\theta}(e_{ij}^{(t)}, \tilde{e}_{ij}) = R_E^t(\tilde{e}_{ij}, e_{ij}^{(t)}) \sum_{e_0} \frac{q_{t|0}(\tilde{e}_{ij} | e_{ij}^{(0)})}{q_{t|0}(e_{ij}^{(t)} | e_{ij}^{(0)})} p_{0|t}^\theta(e_{ij}^{(0)} | G^t)$, for $e_{ij}^{(t)} \neq \tilde{e}_{ij}$
 Sample $j_{e_{ij}^{(t)}, \tilde{e}_{ij}} \sim \mathcal{P}(\tau \hat{R}_E^{t,\theta}(e_{ij}^{(t)}, \tilde{e}_{ij}))$ ▷ Count transitions on edge ij
 end
 end
 for $i = 1$ **to** n **do**
 for \tilde{x} in \mathcal{X} **do**
 if $j_{x_i^{(t)}, \tilde{x}} = 1$ **and** $\sum_{\tilde{x}} j_{x_i^{(t)}, \tilde{x}} = 1$ **then**
 $x_i^{(t-\tau)} = \tilde{x}$ ▷ Apply unique transition or discard
 end
 end
 end
 for $i, j = 1$ **to** n , $i < j$ **do**
 for \tilde{e} in \mathcal{E} **do**
 if $j_{e_{ij}^{(t)}, \tilde{e}} = 1$ **and** $\sum_{\tilde{e}} j_{e_{ij}^{(t)}, \tilde{e}} = 1$ **then**
 $e_{ij}^{(t-\tau)} = \tilde{e}$ ▷ Apply unique transition or discard
 end
 end
 end
 $t \leftarrow t - \tau$
end
 $G^0 \leftarrow \prod_i \operatorname{argmax} p_{0|t}^\theta(x_i^{(0)} | G^{(t)}) \prod_{ij} \operatorname{argmax} p_{0|t}^\theta(e_{ij}^{(0)} | G^{(t)})$ ▷ Last pass
return G^0

Figure 3: Training and Sampling algorithms of COMETH

We use the RRWP encoding, defined in Equation 3, for synthetic graph generation. For molecule generation datasets, we additionally compute several molecular features used in Vignac et al. [2022], namely the valency and charge for each node and the molecular weight.

C Experimental details

Here, we outline the details of your experimental study.

C.1 Synthetic graph generation

We evaluate our method on two datasets from the SPECTRE benchmark [Martinkus et al., 2022], with 200 graphs each. PLANAR contains planar graphs of 64 nodes, and SBM contains graphs drawn from a stochastic block model with up to 187 nodes. We use the same split as the original paper, which uses 128 graphs for training, 40 for training, and the rest as a validation set. Similar to Jo et al. [2024], we apply random permutations to the graphs at each training epoch.

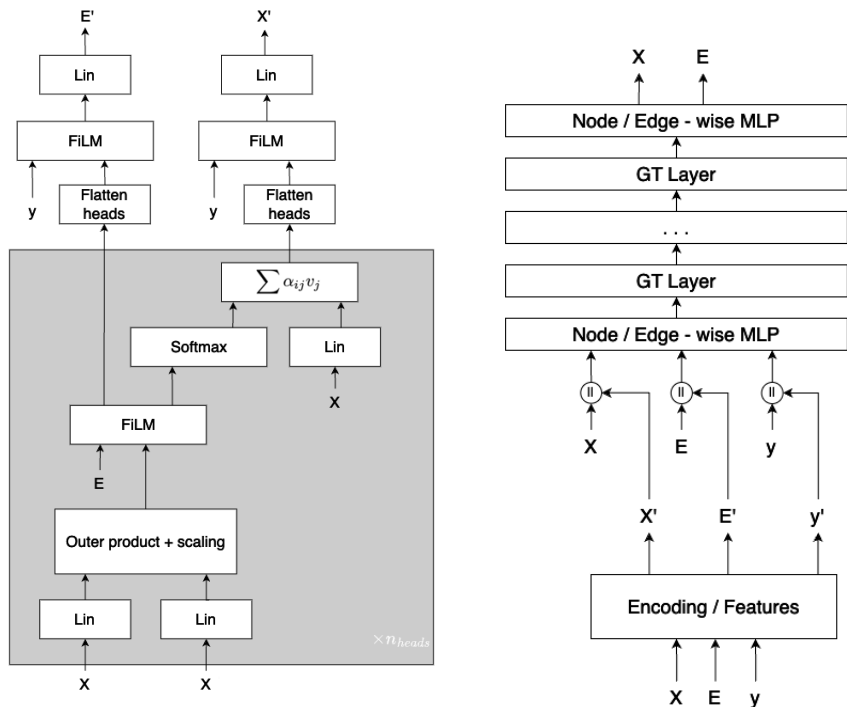


Figure 4: Overview of DIGRESS graph transformer.

We report five metrics from the SPECTRE benchmark, which include four **MMD** metrics between the test set and the generated set and the **VUN** metric on the generated graphs. The MMD metrics measure the **Maximum Mean Discrepancy** between statistics from the test and the generated set, namely the **Degree (Deg.)** distribution, the **Clustering coefficient (Clus.)** distribution, the count of **Orbits (Orb.)** of four nodes and the **eigenvalues (Spec.)** of the graph Laplacian. The **Valid, Unique, and Novel (V.U.N.)** metric measures the percentage of valid, unique, and non-isomorphic graphs to any graph in the training set.

On PLANAR, we report results using $\tau = 0.002$, i.e. using 500 τ -leaping. We also evaluate our model using 10 corrector steps after each predictor step when $t < 0.1T$, with $\tau = 0.002$, for a total of 1000 τ -leaping steps. We found our best results using $\tau_c = 0.7$.

On SBM, we report results using $\tau = 0.001$, i.e. using 1000 τ -leaping steps.

C.2 Small molecule generation : QM9

We evaluate our model on QM9 (Wu et al. [2018]) to assess the ability of our model to model this simple attributed graphs distribution. The molecules are kekulized using the RDKit library and hydrogen atoms are removed, following the standard preprocessing pipeline for this dataset. Edges can have three types, namely simple bonds, double bonds, and triple bonds, as well as one additional type for the absence of edges. The atom types are listed in table 6.

We use the same split as Vignac et al. [2022], i.e., 100k molecules for training, 13k for testing, and the rest (20 885 molecules) as a validation set. We choose this split over the one proposed in Jo et al. [2022] because it leaves a validation set to evaluate the ELBO and select the best checkpoints to minimize this quantity. In consequence, our training dataset contains roughly 20k molecules, which is less than what most graph generation works use.

At the sampling stage, we generate 10k molecules. We evaluate four metrics. The **Validity** is evaluated by sanitizing the molecules and converting them to SMILES string using the RDKit library. The largest molecular fragment is selected as a sample if it is disconnected. We then evaluate the **Uniqueness** among valid molecules. As stated in Vignac et al. [2022], evaluating novelty on QM9 bears little sense

Table 6: Details of the molecular datasets. The number of molecules for GuacaMol is computed after filtration.

Dataset	Number of molecules	Size	Atom types
QM9	133 885	1 to 9	C, N, O, F
MOSES	1 936 962	8 to 27	C, N, S, O, F, Cl, Br
GuacaMol	1 398 223	2 to 88	C, N, O, F, B, Br, Cl, I, P, S, Se, Si

since this dataset consists of an enumeration of all stable molecules containing the atom above types with size nine or smaller. We also evaluate the **Fréchet ChemNet Distance (FCD)**, which embeds the generated set and the test set using the ChemNet neural network and compares the resulting distributions using the Wasserstein-2 distance (Preuer et al. [2018]). Finally, we evaluate the *Neighborhood Subgraph Pairwise Distance Kernel* (NSPDK) between the test set and the generated, which measures the structural similarities between those two distributions.

C.3 Molecule generation on large datasets

We further evaluate COMETH on two large molecule generation benchmarks, MOSES [Polykovskiy et al., 2020] and GuacaMol [Brown et al., 2019]. The molecules are processed the same way as for QM9 and present the same edge types. The atom types for both datasets are listed in table 6. The filtration procedure for the GuacaMol consists of converting the SMILES into graphs and retrieving the original SMILES. The molecules for which this conversion is not possible are discarded. We use the code of Vignac et al. [2022] to perform this procedure. We use the standard split provided for each dataset.

Both datasets are accompanied by their own benchmarking libraries. For GuacaMol, we use the distribution learning benchmark. During the sampling stage, we generate 25k molecules for MOSES and 18k for GuacaMol, which is sufficient for both datasets, as they evaluate metrics based on 10k molecules sampled from the generated SMILES provided.

We then elaborate on the metrics for each dataset. For both datasets, we report **Validity**, defined in the same manner as for QM9, the percentage of **Valid and Unique (Val. & Uni.)** samples, and the percentage of **Valid, Unique, and Novel (V.U.N.)** samples. We prefer the latter two metrics over Uniqueness and Novelty alone, as they provide a better assessment of a model’s performance compared to separately reporting all three metrics (Validity, Uniqueness, and Novelty). The MOSES benchmark also computes metrics by comparing the generated set to a scaffold test set, from which we report the **Fréchet ChemNet Distance (FCD)**, the **Similarity to the nearest neighbor (SNN)**, which computes the average Tanimoto similarity between the molecular fingerprints of a generated set and the fingerprints of the molecules of a reference set, and **Scaffold similarity (Scaf)**, which compares the frequencies of the Bemis-Murcko scaffolds in the generated set and a reference set. Finally, we report the **Filters** metrics, which indicate the percentage of generated molecules successfully passing the filters applied when constructing the dataset. The GuacaMol benchmark computes two *scores*, the **Fréchet ChemNet Distance (FCD)** score and the **KL divergences (KL)** between the distributions of a set of physicochemical descriptors in the training set and the generated set.

We report results using $\tau = 0.002$, i.e., 500 denoising steps on both datasets. The experiments using the predictor-corrector were performed using $\tau = 0.002$ and 10 corrector steps for a total of 500 denoising steps. For both datasets, we used $\tau_c = 1.5$.

C.4 Conditional generation

We perform conditional generation experiments on QM9, targeting two properties, the **dipole moment** μ and the **highest occupied molecular orbital energy (HOMO)**. They are well suited for conditional generation evaluation because they can be estimated using the Psi4 library [Smith et al., 2020].

We trained models sweeping over $p_{\text{uncond}} \in \{0.1, 0.2\}$, and explore different values for s in $\llbracket 1, 6 \rrbracket$ during sampling. We obtained our best results using $p_{\text{uncond}} = 0.1$ and $s = 1$.

During inference, we evaluated our method in the same setting as Vignac et al. [2022]. We sampled 100 molecules from the test set, extracted their dipole moment and HOMO values, and generated 10 molecules targeting those properties. We estimated the HOMO energy and the dipole moment of the

generated molecules, and we report the **Mean Absolute Error (MAE)** between the estimated properties and the corresponding targets.

To efficiently incorporate the conditioner \mathbf{y} , we implemented a couple of ideas proposed in Ninniri et al. [2023]. Instead of using \mathbf{y} solely as a global feature, we incorporated it as an additional feature for each node and edge. Additionally, we trained a two-layer neural network to predict the size of the molecule given the target properties rather than sampling it from the empirical dataset distribution. Our empirical observations indicate that this approach enhances performance.

As of the time of writing, no official implementation has been released for Ninniri et al. [2023], rendering it impossible to reproduce their results. Additionally, since they do not report validity in their experiments on QM9, we choose not to include their results as a baseline to avoid unfair comparisons.

C.5 Compute Ressources

Experiments on QM9, Planar, and SBM were carried out using a single V100 or A10 GPU at the training and sampling stage. We trained models on MOSES or Guacamol using three A100 GPUs. To sample from these models, we used a single A100 GPU.

D Limitations

Although our model advances the state-of-the-art across all considered benchmarks, it still faces quadratic complexity, a common issue in graph diffusion models. This problem could be alleviated by adapting methods like EDGE [Chen et al., 2023] used to scale DiGRESS for large graph generation. Additionally, our approach does not support the generation of continuous features and is restricted to categorical attributes. To generate continuous features, it should be combined with a continuous-state diffusion model, resulting in an approach similar to Vignac et al. [2023].

E Samples

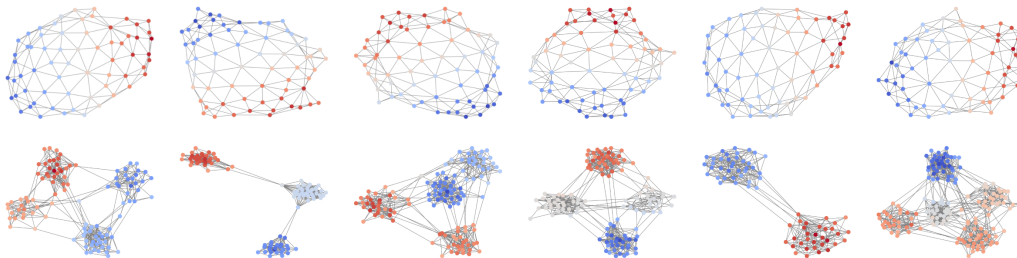


Figure 5: Samples from PLANAR on Planar (top) and SBM (bottom)

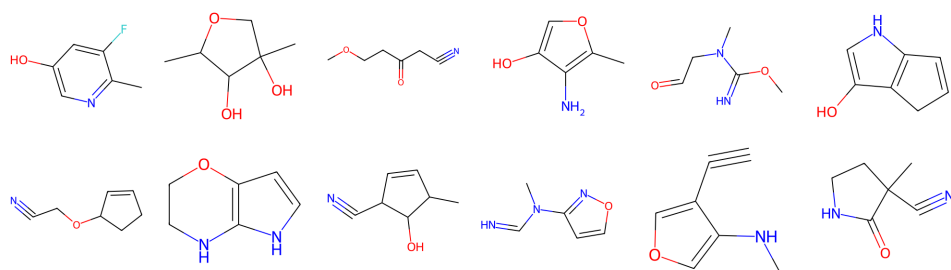


Figure 6: Samples from COMETH on QM9.

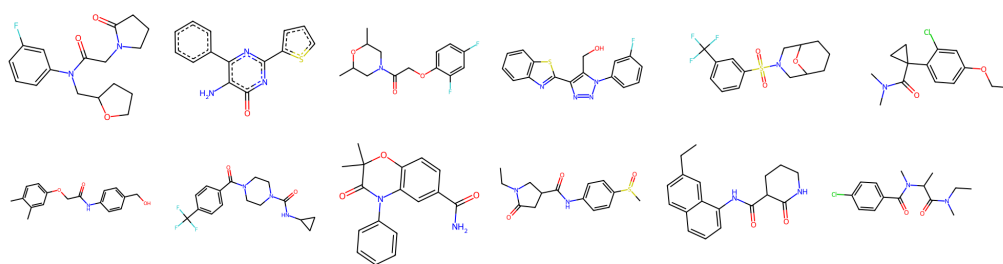


Figure 7: Samples from COMETH on MOSES.

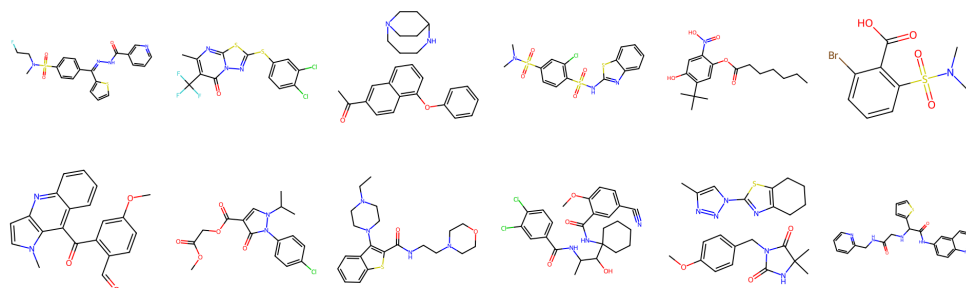


Figure 8: Samples from COMETH on GuacaMol. The samples on this dataset exhibit some failure cases, such as disconnected molecules or 3-cycles of carbon atoms.